

2D Materials



PAPER

Uniaxial compression of suspended single and multilayer graphenes

RECEIVED
2 February 2016

REVISED
19 May 2016

ACCEPTED FOR PUBLICATION
31 May 2016

PUBLISHED
10 June 2016

A P Sgouros^{1,2,3}, G Kalosakas^{1,3,4}, C Galiotis^{1,5} and K Papagelis^{1,3}

¹ Institute of Chemical Engineering Sciences—Foundation of Research and Technology Hellas (FORTH/ICE-HT), GR-26504 Patras, Greece

² School of Chemical Engineering, National Technical University of Athens (NTUA), GR-15780 Athens, Greece

³ Department of Materials Science, University of Patras, GR-26504 Patras, Greece

⁴ Crete Center for Quantum Complexity and Nanotechnology (CCQCN), Physics Department, University of Crete GR-71003 Heraklion, Greece

⁵ School of Chemical Engineering, University of Patras, GR-26504 Patras, Greece

E-mail: georgek@upatras.gr

Keywords: graphene, uniaxial compression, critical buckling, molecular dynamics

Supplementary material for this article is available [online](#)

Abstract

The mechanical response of single and multiple graphene sheets under uniaxial compressive loads was studied with molecular dynamics (MD) simulations, using different semi-empirical force fields at different boundary conditions or constrains. Compressive stress–strain curves were obtained and the critical stress/strain values were derived. The MD results are compared to the linear elasticity continuum theory for loaded slabs. Concerning the length dependence of critical values, qualitatively similar behavior is observed between the theory and numerical simulations for single layer graphenes, as the critical stress/strain for buckling was found to scale to the inverse squared length. However discrepancies were noted for multilayer graphenes, where the critical buckling stress also decreased with increasing length, though at a slower rate than expected from elastic buckling analysis.

1. Introduction

Graphene is an ultrathin membrane of atomic thickness that possesses exceptional electronic [1, 2], thermal [3–5] and mechanical properties [6] which far exceed those of conventional 3D materials. Graphene being the first two-dimensional material discovered [7], due to its unique properties could form a basis for numerous applications in several branches of technology, such as in polymer matrix composite materials [8–11], optoelectronics [12, 13], drug delivery [14–16], super capacitors [17] and many more. By applying stress or strain on graphene (the so called ‘strain engineering’) one can modify its electronic properties [18], and this can make an impact to numerous applications, ranging from strain sensors [19, 20] to electric circuits made from graphene [21]. Graphene ribbons under compressive loads fail by the formation of wrinkles, the wavelength, amplitude and direction of which can be controlled by modifying the boundary conditions along their edges [22]. Those wrinkles can affect drastically the local fields and the electronic

properties by inducing effective magnetic fields [23, 24].

The experimental Young’s modulus and tensile intrinsic strength of graphene have been estimated to 1 TPa and 130 GPa, respectively, by nanoindenting suspended graphene sheets with an AFM tip [6]. Another method for inducing tensile (compressive) strain to graphene is by placing graphene flakes on plastic beams [11, 25–27], and then, by bending the beams [28], strains up to $\varepsilon_t \sim 1.5\%$ ($\varepsilon_c = 0.7\%$) have been achieved [29]. Graphene of monoatomic thickness freely suspended in air is expected to have extremely low resistance to compressive loading. However, the usage of substrate can drastically change the mechanical properties of graphene, since the critical buckling strain of supported graphenes can be orders of magnitude higher than suspended graphenes [11]. This behavior is indeed very important since it confirms the role of graphene as a reinforcing agent in composite applications.

The mechanical behavior under uniaxial compression of single layer graphene (SLG) has been

investigated in a few theoretical works, using molecular mechanics [30], molecular dynamics (MD) simulations [31–33] and continuum mechanics [34]. The critical buckling stress/strain of SLG has been found to scale inversely proportional to the square of its length [30, 32, 33], in agreement with the linear elasticity theory of loaded slabs [35]. Additionally it has been found [30, 33] that the critical buckling strain is the same for uniaxial compression along either the zigzag or the armchair directions. Similar theoretical studies of uniaxial compression on multilayer graphene (MLG) are limited; a finite element approach has been used for the buckling instability of bilayer graphene [36].

In this work we performed MD simulations in order to study the mechanical response of suspended SLG and MLG under constant compressive loads (stress controlled simulations). Different semi-empirical force fields are used in order to verify the robustness of the observed behavior. The main results obtained from our simulations were the compressive stress–strain curves. The critical buckling stress (σ_{crit}) and strain ($\varepsilon_{\text{crit}}$), the Young's modulus (E) and the Poisson's ratio (ν) were calculated. The critical buckling values presented here concern intrinsic properties of suspended graphenes. As mentioned above, the corresponding values for graphenes embedded in matrices, or supported on beams are expected to be significantly larger. The results of the simulations regarding the critical buckling values were compared with the linear elasticity theory for wide plates with unsupported sides under uniaxial compressive forces. We find that the continuum elasticity theory fails to describe the behavior observed in MLGs.

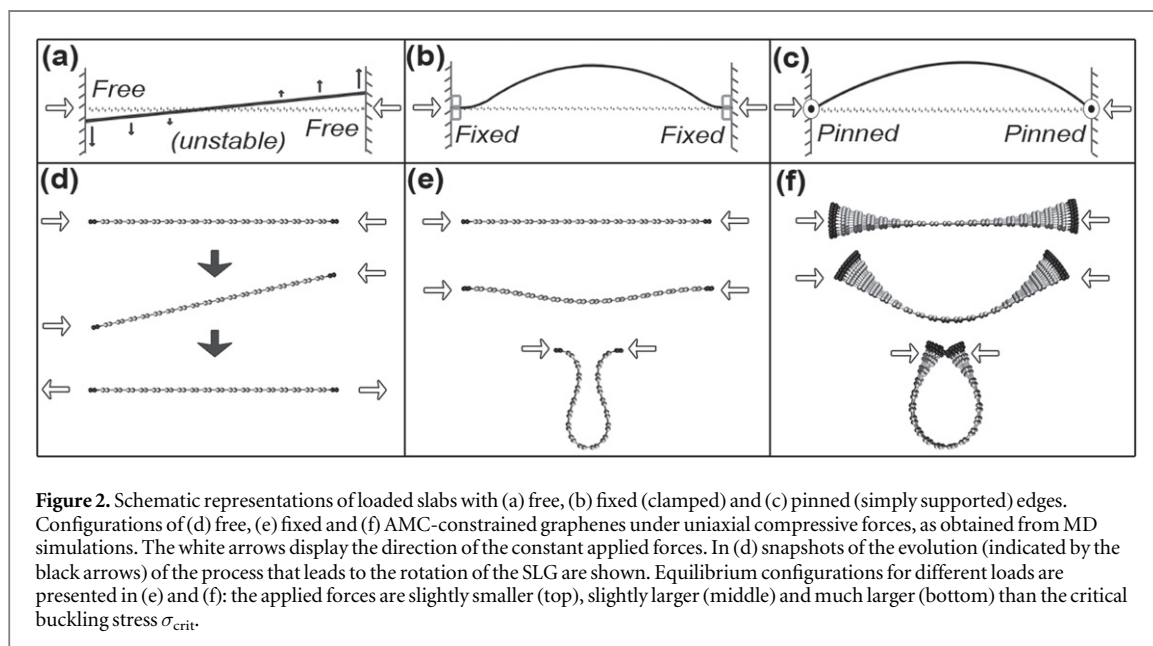
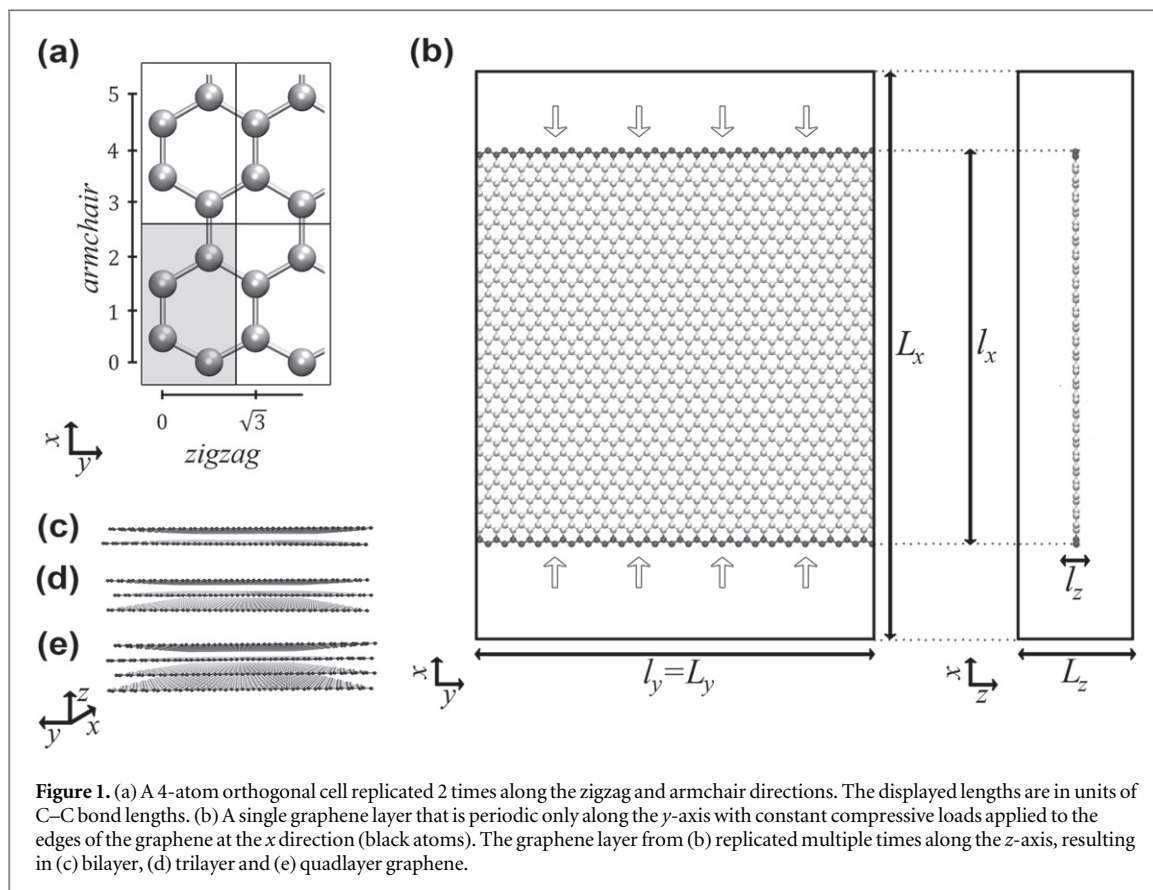
2. Methods

The MD simulations were performed with the LAMMPS package [37, 38] in the isobaric–isothermal ensemble using periodic boundary conditions and a time step equal to 1 fs. In this study we present extensive results for SLGs and MLGs (up to six layers) for various lengths at low temperatures. The temperature (pressure) of the system was maintained constant to 1 K (0 bar) using the Nosé–Hoover thermostat (barostat) [39, 40] with an effective relaxation time equal to 0.1 ps (1 ps). Simulations have also been performed at room temperature for single layer and bilayer graphenes and qualitatively similar results were found as those presented here; however, the data showed a considerable scatter and longer relaxation times are normally needed. We note that the dimensions of the studied graphenes (see below) at 1 K are larger than the characteristic thermal length at this temperature (around 2.5 nm), representing the length scale above which thermal fluctuations become important [41].

To obtain force field independent results, calculations were performed for SLGs with three semi-empirical potentials: the Tersoff [42, 43], the REBO [44] and the LCBOP I [45]. Since we found qualitatively similar behavior for these potentials concerning the length dependence of the critical buckling values, for the computationally more intensive case of MLGs we used the LCBOP potential, though some example cases were checked with the AIREBO [46] potential as well. It has been shown that the LCBOP potential provides a relatively accurate overall description of the phonon dispersion in graphene [47]. The atomistic representations and the data visualization were aided with relevant software [48, 49].

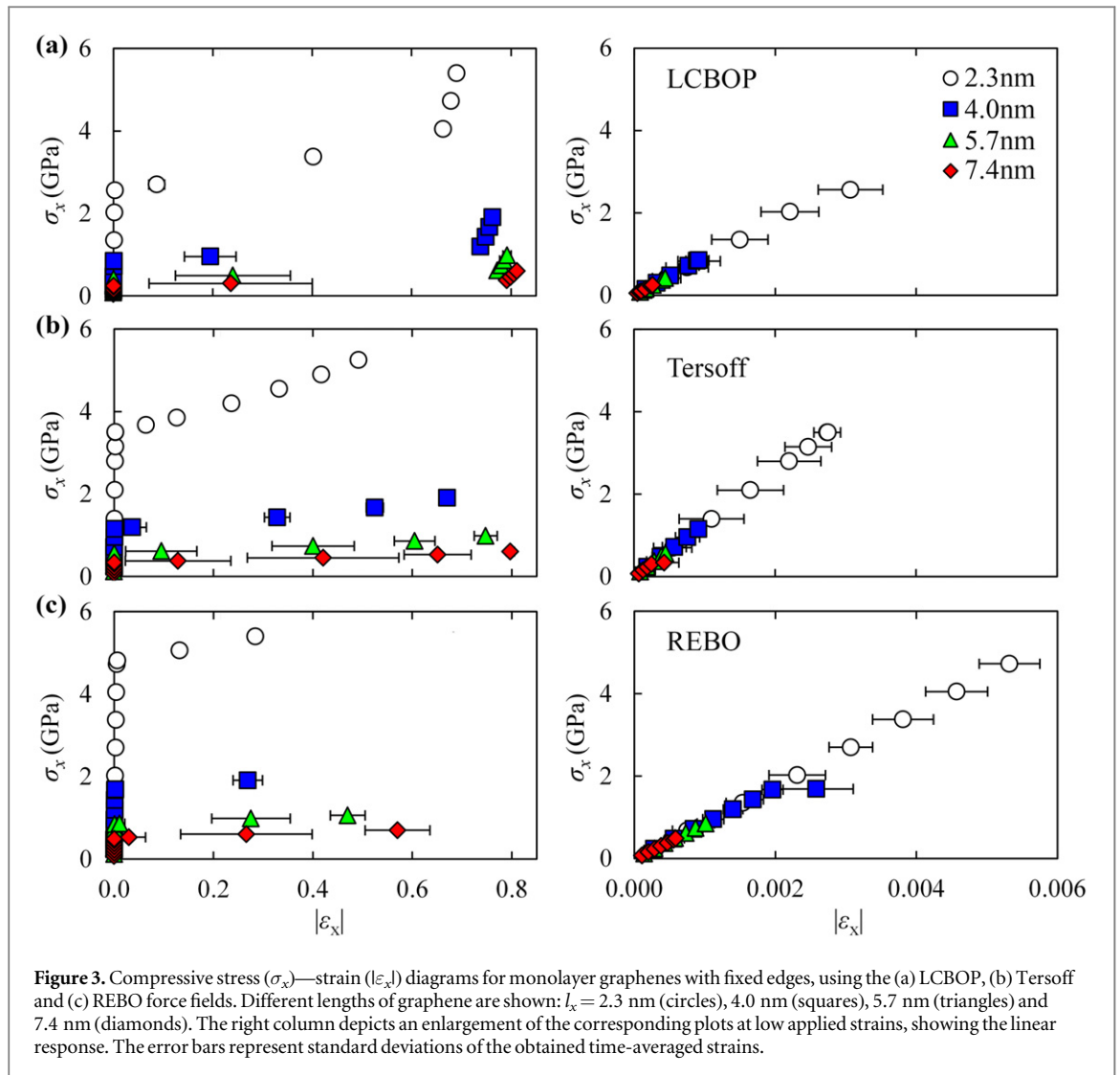
In order to design the graphene sheets, the 4-atom orthogonal cell in figure 1(a) was duplicated several times along the armchair and zigzag directions. Figure 1(b) displays a SLG with dimensions l_x (length), l_y (width) and l_z (thickness) inside a simulation box with dimensions L_x , L_y and L_z , where $l_x < L_x$, $l_y = L_y$ and $l_z < L_z$. The typical dimensions of the graphene sheets studied in this work had lengths (l_x) 2.3–85 nm and widths (l_y) 6 nm, while the vacuum gap along the x - and z -axis was set to about 10 nm. The thickness of SLGs was assumed to be equal to the interlayer distance of MLG, $l_z = 0.335$ nm [50, 51]. In order to avoid spurious interactions along the directions of x - and z -axis the differences $L_x - l_x$ and $L_z - l_z$ were larger than the cut off distance of the used potentials, hence our system was periodic only along the y -axis direction as it is illustrated in figure 1(b). In practice, this means that our results concern graphenes of relatively large widths. By replicating the graphene sheets along the z -axis direction, MLGs with up to 6 layers were constructed (as shown in figures 1(c)–(e) for 2, 3 and 4 layers, respectively). It should be noted that the AB stacking was found to be stable in contrast to the case of AA stacking, in accordance with [52].

The applied constraints at the loading edges of graphene play an important role to its mechanical response, as it has been demonstrated by continuum models [35, 53]. In the case where no geometrical constraints are applied (free edges) the graphene sheets can simply rotate under compressive uniaxial loads, as it is illustrated in the schematic of figure 2(a) and the atomistic representation of a MD simulation in figure 2(d). One way to prevent rotations of the graphenes in MD is to constrain the edges of graphene in the xy -plane (fixed edges, see figure 2(e)). The behavior of those systems corresponds to the case of slabs with clamped (fixed) edges in the continuum model (see schematic of figure 2(b)), since in both cases the displacement w of the edges along the z -axis and its derivative (dw/dx) equal to zero [35]. Another method implemented in LAMMPS [38] to prevent rotations of a nanostructure is to maintain its angular momentum to zero, by subtracting at each time step of the simulation from each atom the average angular velocity with respect to the center of mass. In this case, the



graphenes under the compressive forces were bended as shown in figure 2(f). This condition will be referred as ‘angular momentum conserving’ (AMC) constrain. It should be noted that this approach cannot be applied effectively to graphenes where l_y is much larger than l_x since they are able to respond by twisting instead of bending (see for example the figure S1 in the supplementary material information). AMC constrained graphenes feature a shape similar with that of

pinned plates at the edges, in the sense that the displacement w exhibits an almost linear behavior near the edges indicating that $d^2w/dx^2 \approx 0$. In plates with pinned edges the displacement w and its second derivative (d^2w/dx^2) at their edges are zero (see schematic of figure 2(c)). One strict difference is that in AMC the displacements w of the edges are not zero. However, due to AMC and the symmetry of the structure, the relative displacement between the two edges of



graphene is zero, as happens with the case of pinned plates. Graphenes with either fixed edges or under AMC constrains are considered in the MD simulations here.

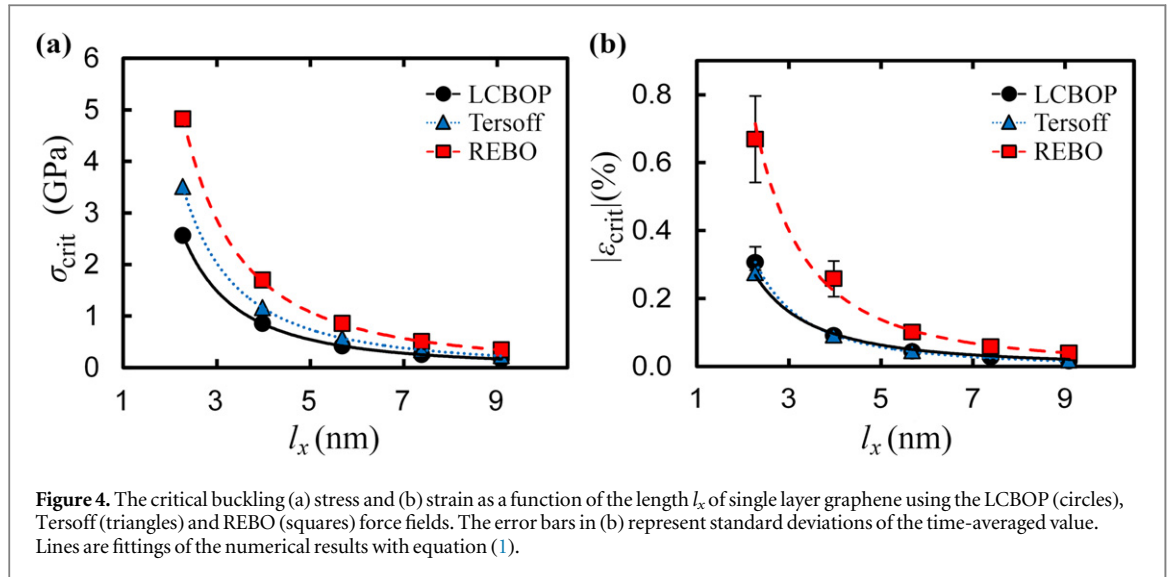
Initially, the graphenes free of any load were left to relax for 100 ps to achieve equilibrium at the desired temperature and pressure, and acquire the initial dimensions. Next, compressive forces of constant magnitude were applied to the atoms at the edges of graphene (black atoms in figure 1(b)) for up to 10 ns. We have tested that this time is sufficient for achieving time independent results for the considered cases. The obtained strain was calculated by time averaging the value of the strain during the last 0.5 ns of the simulation. By performing MD simulations for a wide range of the applied forces, the stress–strain curves were extracted. We have checked that the depth of the region of atoms that are constrained in-plane in the case of fixed edges, does not affect the response of the graphenes as long as the distance between those regions (the effective length of graphene) remains constant.

3. Results and discussion

3.1. Uniaxial compression of monolayer graphene

Figure 3 displays the compressive stress–strain curves of SLGs with different lengths l_x using the boundary condition of fixed edges for the three different force fields. In the limit of small strains the Young’s modulus (Poisson’s ratio) was calculated to ~ 0.93 TPa (0.2), 1.26 TPa (-0.1) and 0.86 TPa (0.3) for the LCBOP, Tersoff and REBO force fields, respectively.

The value of the obtained elastic modulus is more or less close to the experimental value of 1.0 ± 0.1 TPa [6] for the LCBOP and REBO potentials, while the Tersoff overestimates it. The Poisson’s ratios in the LCBOP and REBO cases are also in agreement with other calculations [54–57]. The negative Poisson ratio obtained by the Tersoff potential is an artifact that has been reported in literature [58] and can be attributed to inaccuracies of the potential. As it can be seen from figure 3, the behavior of the stress–strain curves is qualitatively similar for all the tested potentials. Above a critical stress value the strain abruptly increases



indicating the buckling of graphene. The critical buckling value depends on the length l_x of graphene.

Figures 4(a) and (b) present the critical buckling stress and strain with respect to the length l_x of graphene for the three force fields used. The critical buckling stress was calculated with a resolution lower than 0.01 GPa (the corresponding error bars in figure 4(a) are negligibly small). The critical buckling strain equals to the value of strain just before the buckling instability (see the figure S2(a) in the supplementary material). For all the used force fields, the length dependence of the critical values σ_{crit} and $\varepsilon_{\text{crit}}$ are accurately described by an inverse square law:

$$\sigma_{\text{crit}} = \frac{\alpha}{l_x^2}, \quad \varepsilon_{\text{crit}} = \frac{\alpha'}{l_x^2}, \quad (1)$$

where α and α' are constants. This is in agreement with [30, 32, 33] where the critical buckling values were found to be inversely proportional to the length square. As we examined periodic systems in the direction of y -axis, simulations at different values of l_y , up to 25 nm, show no dependence of the critical buckling values on l_y , at least for the low temperatures considered here.

Qualitatively, the behavior of SLGs under the AMC constrain was quite similar with that of SLGs with fixed ends. This can be seen from figures S3 and S4 in the supplementary material information, which display the stress–strain diagram and the plots of σ_{crit} and $\varepsilon_{\text{crit}}$ versus l_x respectively, for this case using the LCBOP potential. However, the critical buckling stress was found to be about 3–4 times smaller than the corresponding value calculated for SLG with fixed ends, a result that is related with continuum models (see below).

Figure 5 displays the variation of the C–C bond lengths along the loading direction (x -axis) for a fixed-edged SLG with $l_x = 2.7$ nm, for various values of the applied force above the critical buckling σ_{crit} , using the LCBOP force field. The C–C bonds in graphenes that

are not subjected to compressive loads (figure 5, black circles) are equal to 1.42 Å in the central region of the sheet and about 1.6% larger at the boundary due to edge effects. However graphene sheets under loads that exceed the σ_{crit} value (onset of buckling) show an increase of the bond length near the central region. This is in accordance with the observed relaxation of the frequency shift of certain Raman bands after the onset of buckling of monolayer graphene [29, 59].

The critical buckling strains ($\varepsilon_{\text{crit}}$) were found to be the same along the armchair and zigzag directions of graphene in [30, 33]. In the current study graphene sheets with loading direction at various angles were examined, in order to investigate the dependence of σ_{crit} on the chiral angle (θ_{chiral}) of the applied stress. It should be noted that the chiral angle can only take specific values in order to maintain proper periodicity of the lattice along the periodic boundaries of the simulation box. Figure 6 displays results of σ_{crit} for graphene sheets with $l_x \approx 4$ nm (circles) and $l_x \approx 7$ nm (triangles), uniaxially compressed at different chiral angles θ_{chiral} using the LCBOP potential. In both cases $l_y = 6$ nm. These results are in agreement with [30] where the REBO potential was used in molecular mechanics simulations and the critical buckling was found insensitive to the chirality of the loading direction.

3.2. Uniaxial compression of multilayer graphene

Here, the compressive response of MLGs is discussed, through MD simulations using the LCBOP force field. Figure 7 shows that the stress–strain curves of MLGs with fixed edges exhibit a similar behavior with that of SLGs (see figure 3). The buckling instability in this case is similar to that occurring in SLGs, as can be seen from figure S2(b) in the supplementary material section. In all presented cases, the Young's modulus was calculated in the regime 0.90–0.95 TPa.

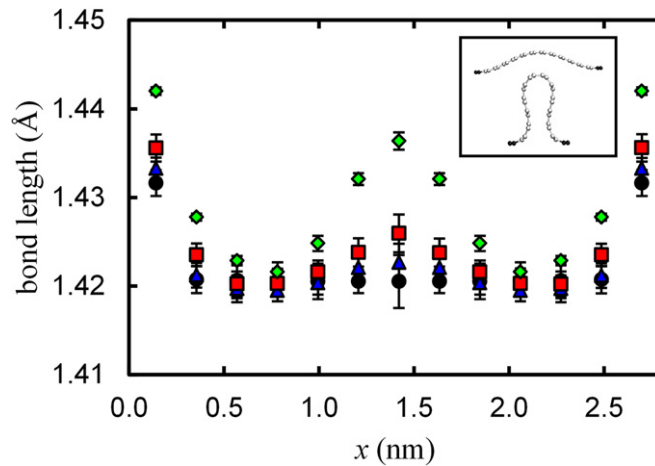


Figure 5. Variation of the C–C bond lengths along the loading direction for graphene sheets with $l_x = 2.7$ nm under compressive uniaxial loads equal to 0.0 (circles), 2.1 (triangles), 2.3 (squares) and 2.5 (diamonds) GPa. In this case $\sigma_{\text{crit}} = 1.8$ GPa. The inset displays two graphene equilibrium configurations with $\sigma_x = 2.1$ GPa (top) and $\sigma_x = 2.5$ GPa (bottom). The error bars represent standard deviations of the time- and width-averaged values shown in the figure.

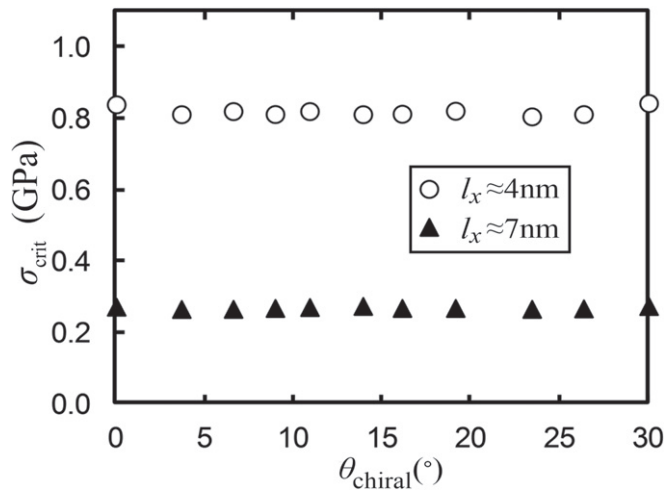


Figure 6. The critical buckling stress σ_{crit} versus the chiral angle (θ_{chiral}) of the loading direction for graphene sheets with $l_x \approx 4$ nm (circles) and $l_x \approx 7$ nm (triangles).

As expected, for $\sigma > \sigma_{\text{crit}}$, there seems to be an increased resistance of the sheets for further bending as the number N of layers increases. For example, for sheets with length $l_x = 2.3$ nm, when $\sigma_x = 4$ GPa the ε_x of SLG is about 65% (derived from the data shown in figure 3(a) with circles), while the corresponding one of MLGs with $N = 2, 3$ and 4 layers is about $\varepsilon_x = 25\%$, 17% and 10% (derived from the data shown with circles in figures 7(a)–(c), respectively). Similar behavior occurs for other values of l_x .

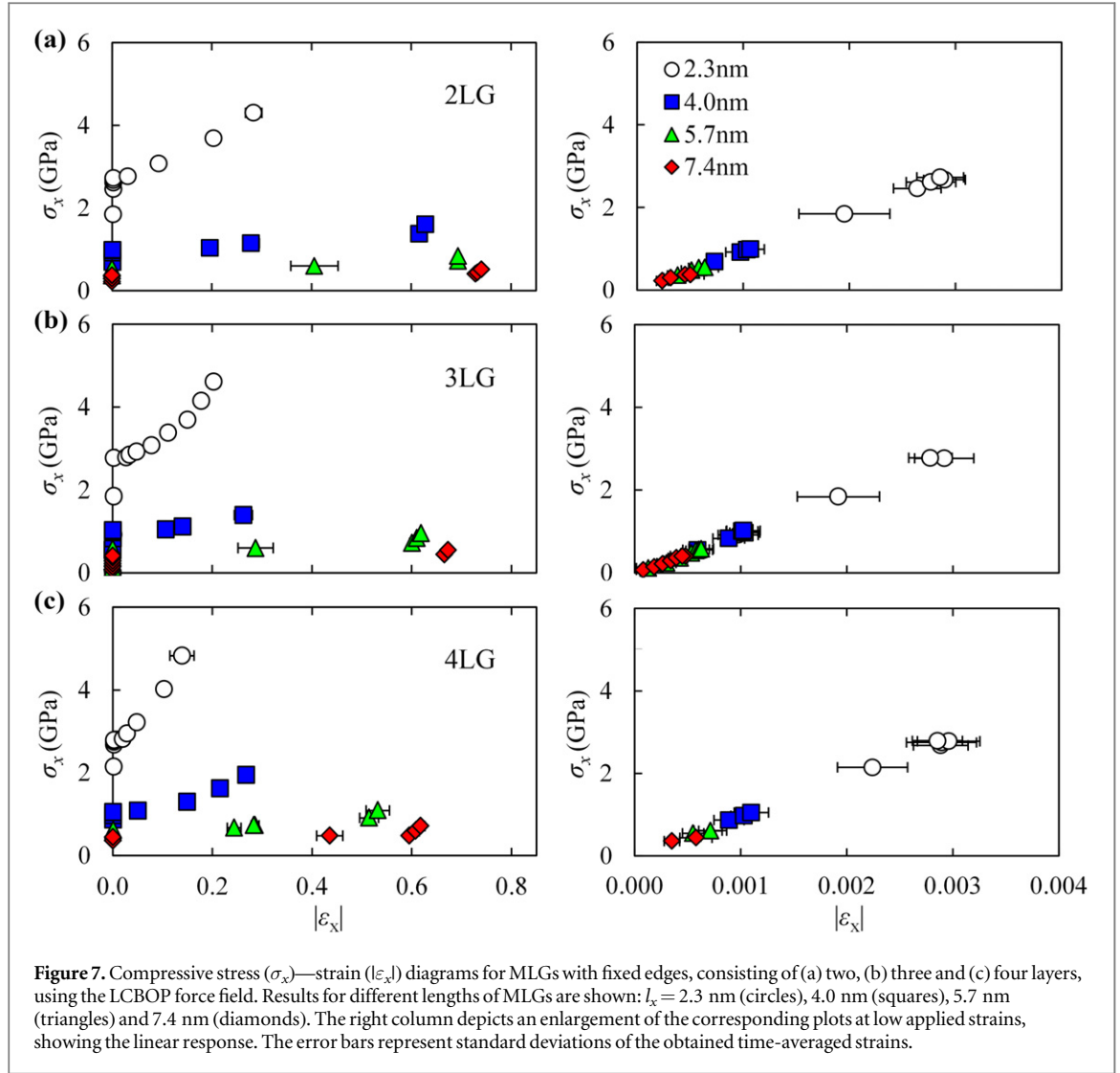
The critical buckling stress σ_{crit} as a function of the length l_x of MLGs with fixed edges and unsupported sides is presented in figure 8, for $N = 2$ up to $N = 6$ layers. The SLG case with $N = 1$ (circles in figure 4(a)) is also shown for comparison. The solid line shows the fitting of SLG results with the inverse square law, equation (1). Figure 8(a) clearly demonstrates that the critical buckling stresses of MLGs do not follow an inverse square law, but they exhibit a slower decrease

with the length that can not be described through a simple power law. Similar results have been obtained for bilayer graphenes ($N = 2$) using the AIREBO potential as well (see figure S5 in the supplementary material).

Multilayers under the AMC constrain displayed a similar behavior, regarding the σ_{crit} dependence on l_x , as illustrated in figure S6 of the supplementary information. Additionally, for AMC-constrained MLGs, the σ_{crit} is about 2–4 times smaller than the corresponding σ_{crit} value of MLGs with fixed ends.

3.3. Comparison with the linear elasticity theory for loaded slabs

In the linear elasticity theory of continuum mechanics, the critical buckling stress of a wide plate with unsupported sides, length l_x , thickness l_z , Poisson's ratio ν and Young's modulus E is provided from the



following relation [35]:

$$\sigma_{\text{crit}} = \frac{\pi^2}{12} \frac{E}{1 - \nu^2} \frac{l_z^2}{(l_x/p)^2} = \frac{d}{(l_x/p)^2}, \quad (2)$$

where $p = 2$ for slabs with fixed edges, while $p = 1$ for slabs with pinned edges. This difference in the value of p results in $\sigma_{\text{crit}}^{\text{fix}} = 4 \cdot \sigma_{\text{crit}}^{\text{pin}}$, where $\sigma_{\text{crit}}^{\text{fix}}$ ($\sigma_{\text{crit}}^{\text{pin}}$) is the critical buckling stress for plates with fixed (pinned) edges. Note that the equation (1) of [11] giving the critical buckling value for plates with simply supported sides, is reduced for wide plates to the $1/l_x^2$ dependence of equation (2), taking into account that when the width w is much larger than the length l , then the geometric term K tends to w^2/l^2 . Moreover, the same equation contains the thickness dependence ($\sim l_z^2$) appeared in equation (2), considering that the ratio D/C of the flexural and tension rigidities equals to $h^2/12$ (see equation (2) of [29]), where h is the thickness of the plate. For wide plates such a coincidence of formulae corresponding to different boundary conditions at the sides of the plate is expected, since in this case (where the width is very large) the boundaries at the sides play a negligible role.

The results from the MD simulations in SLGs are in qualitative agreement with the continuum model since they give $\sigma_{\text{crit}} \propto l_x^{-2}$ (see figure 4(a) and equation (1) or figure 8(a)). However, there is a discrepancy at a quantitative level: for a SLG with $E = 1$ TPa [6], $l_z = 0.335$ nm [50] and $\nu = 0.22$ [54], the constant d in equation (2) equals to 97 GPa nm², which is much larger than the value extracted from the MD simulations. The continuum model could be fitted to the results derived from the MD simulations by adjusting the conventional thickness of the SLG ($l_z = 0.335$ nm) to an effective thickness that equals to about 0.04 nm. Such an unrealistic requirement for the graphene thickness, in order to fit atomistic results with the predictions of the continuum theory for plates, also appears in the case of graphene bending [60]. We also note that the ratio $\sigma_{\text{crit}}^{\text{f}}/\sigma_{\text{crit}}^{\text{AMC}}$ of the critical values for fixed-edged and AMC-constrained (which show some analogy with the behavior of pinned edges as discussed in section 2) SLGs is close to 4 as it is displayed in figure 9.

In the case of MLGs qualitatively different behaviors are obtained between the results of MD

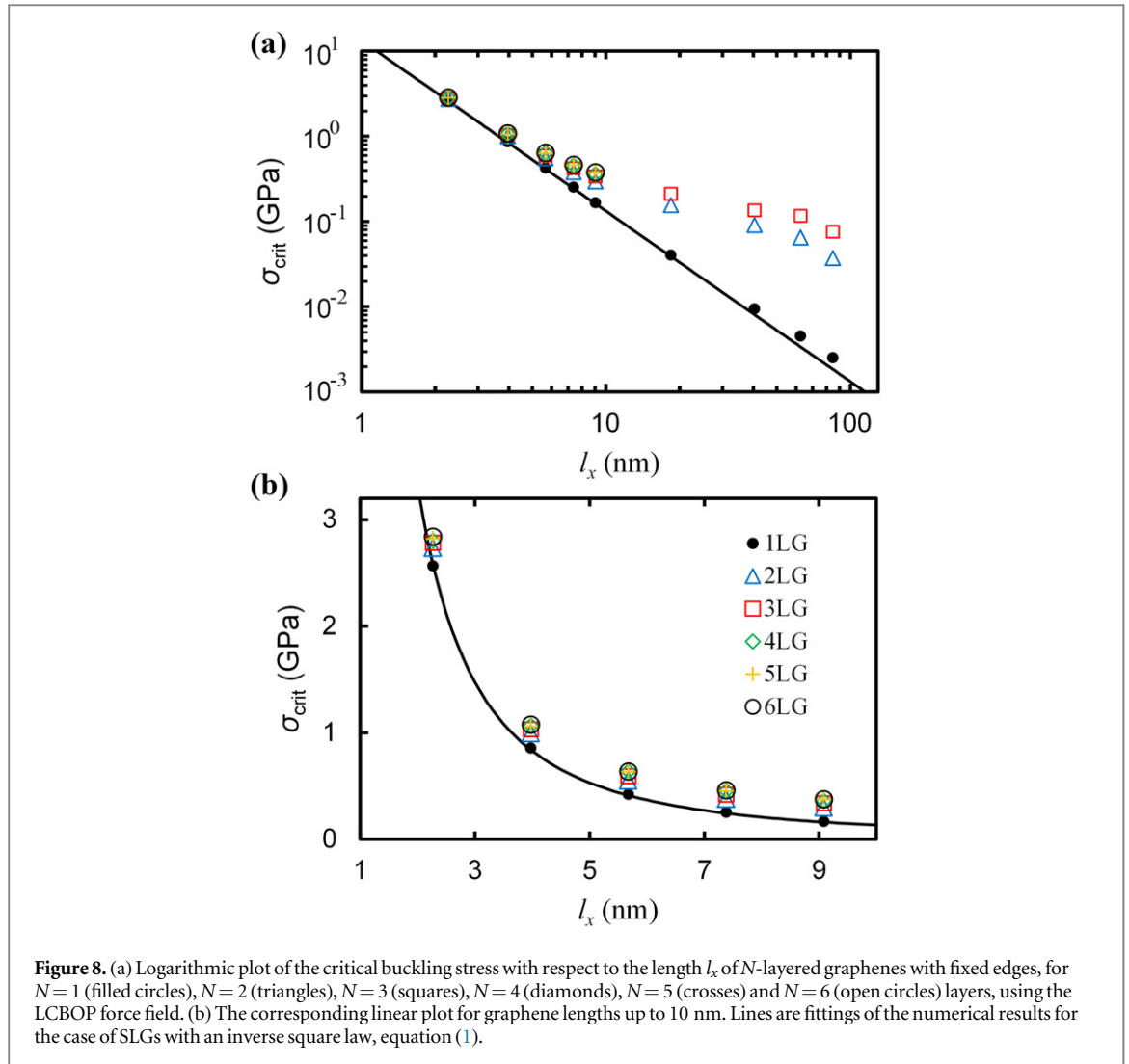


Figure 8. (a) Logarithmic plot of the critical buckling stress with respect to the length l_x of N -layered graphenes with fixed edges, for $N=1$ (filled circles), $N=2$ (triangles), $N=3$ (squares), $N=4$ (diamonds), $N=5$ (crosses) and $N=6$ (open circles) layers, using the LCBOP force field. (b) The corresponding linear plot for graphene lengths up to 10 nm. Lines are fittings of the numerical results for the case of SLGs with an inverse square law, equation (1).

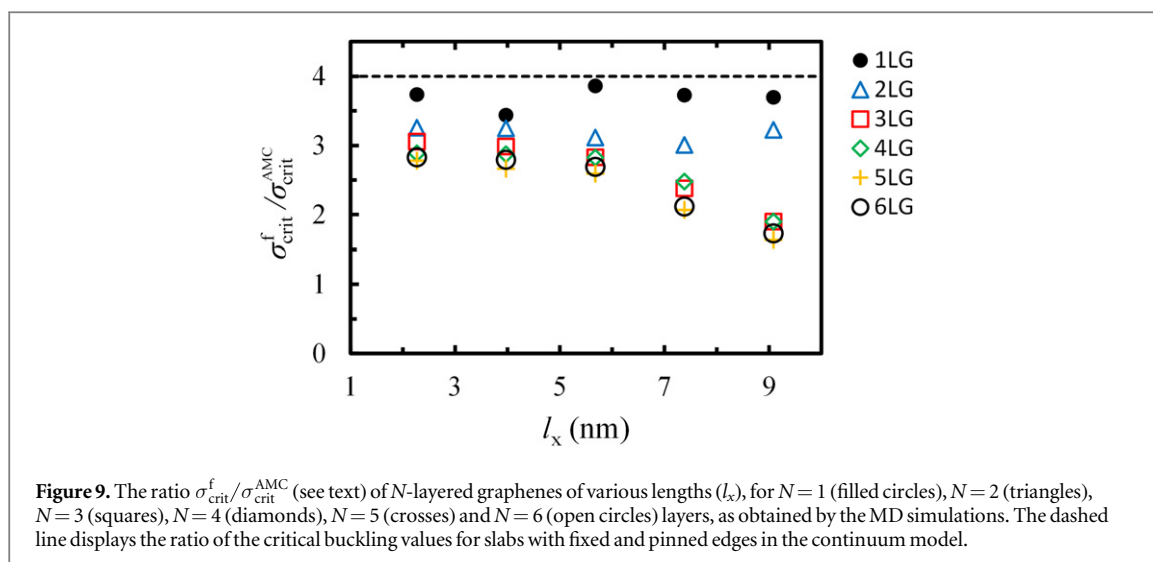
simulations and the continuum theory for loaded slabs with unsupported sides. In particular, as figure 8(a) shows, the MD calculations reveal significant deviations from the $1/l_x^2$ law of equation (2), concerning the length dependence of critical buckling values. Moreover, in the linear elasticity continuum theory the σ_{crit} is proportional to the square of the plate thickness l_z (see equation (2)), while the MD simulations show that σ_{crit} only slightly increases with l_z , as can be seen from figure 8(b). Both fixed edged and AMC constrained graphenes reveal these features in the numerical simulations. The ratio $\sigma_{\text{crit}}^f/\sigma_{\text{crit}}^{\text{AMC}}$ for MLGs is also shown in figure 9.

In MLGs the obtained MD results, concerning the σ_{crit} variation with the graphene length, are due to their discrete nature and the interlayer interactions. Modifying the interlayer interactions, affects the length dependence of critical buckling. This is demonstrated in figure S7 of the supplementary information for graphene bilayers. In this case the interlayer interaction is described through interatomic Lennard–Jones potentials and we have varied the depth ε of the Lennard–Jones potential from tenths up to hundreds of the corresponding normal value [61]. As expected,

when the strength of the interlayer interaction decreases, the results tend to those of the SLG case, depicted also in figure S7 for comparison. By increasing the strength of this interaction, the behavior of σ_{crit} changes and the exponent of the power law that was fitted to the data decreases towards the value -2 (at least for the lengths shown in figure S7).

4. Conclusions

The behavior of single layer and multilayer graphenes of large width under uniaxial compressive loads was investigated, through MD simulations. The compressive tests were stress-controlled and the simulations took place in the isothermal–isobaric ensemble. The studied graphene sheets in this work had typical dimensions of length $2 \text{ nm} < l_x < 100 \text{ nm}$ and thickness $l_z \approx 0.3\text{--}2 \text{ nm}$ (from one up to six graphene layers), while periodic boundary conditions were used along the y direction. Different force fields and boundary conditions/constraints were used in our MD simulations. For SLGs the calculated elastic moduli were relatively close to the experimental value



$E = 1$ TPa, while the Poisson ratios of the LCBOP and REBO potentials were in the range 0.2–0.3, in agreement with values reported in the literature.

For SLGs, the critical buckling stress/strain is inversely proportional to the square of the length of graphene along the loading direction. Additionally, the σ_{crit} was found to be independent on the loading direction (armchair, zigzag or any other chiral direction). The MD results for SLGs show qualitative agreement with the continuum theory for uniaxial compressive deformation of wide plates of unsupported sides.

However, in the case of MLGs discrepancies were found between the MD calculations and the continuum linear elasticity theory. The latter one predicts that σ_{crit} increases with the square of the thickness, while the MD simulations show a significantly smaller increase. Furthermore, the inverse squared length dependence of the critical buckling values, as anticipated in the continuum theory for plates, is not verified by the numerical simulations, where deviations from this behavior are obtained for MLGs with $N = 2$ up to $N = 6$ layers.

Acknowledgments

We would like to thank D N Theodorou and C Tzoumanekas for valuable discussions. This work has been partially supported from the Thales project GRAPHENECOMP co-financed by the European Union (ESF) and the Greek Ministry of Education (through ΕΣΠΙΑ program), and by European Union's Seventh Framework Programme (FP7-REGPOT-2012-2013-1) under grant agreement n° 316165. Financial support of Graphene FET Flagship (Graphene-Based Revolutions in ICT and Beyond, Grant No. 604391) is also acknowledged.

References

- [1] Novoselov K S, Geim A K, Morozov S V, Jiang D, Katsnelson M I, Grigorieva I V, Dubonos S V and Firsov A A 2005 Two-dimensional gas of massless Dirac fermions in graphene *Nature* **438** 197–200
- [2] Zhang Y, Tan Y-W, Stormer H L and Kim P 2005 Experimental observation of the quantum Hall effect and Berry's phase in graphene *Nature* **438** 201–4
- [3] Cai W, Moore A L, Zhu Y, Li X, Chen S, Shi L and Ruoff R S 2010 Thermal transport in suspended and supported monolayer graphene grown by chemical vapor deposition *Nano Lett.* **10** 1645–51
- [4] Faugeras C, Faugeras B, Orlita M, Potemski M, Nair R R and Geim A K 2010 Thermal conductivity of graphene in corbino membrane geometry *ACS Nano* **4** 1889–92
- [5] Balandin A A, Ghosh S, Bao W, Calizo I, Teweldebrhan D, Miao F and Lau C N 2008 Superior thermal conductivity of single-layer graphene *Nano Lett.* **8** 902–7
- [6] Lee C, Wei X, Kysar J W and Hone J 2008 Measurement of the elastic properties and intrinsic strength of monolayer graphene *Science* **321** 385–8
- [7] Geim A K 2011 Random walk to graphene (Nobel lecture) *Angew. Chem., Int. Ed. Engl.* **50** 6966–85
- [8] Stankovich S, Dikin D A, Dommett G H B, Kohlhaas K M, Zimney E J, Stach E A, Piner R D, Nguyen S T and Ruoff R S 2006 Graphene-based composite materials *Nature* **442** 282–6
- [9] Ramanathan T et al 2008 Functionalized graphene sheets for polymer nanocomposites *Nat. Nanotechnol.* **3** 327–31
- [10] Rafiee M A, Rafiee J, Yu Z Z and Koratkar N 2009 Buckling resistant graphene nanocomposites *Appl. Phys. Lett.* **95** 223103
- [11] Frank O, Tsoukleri G, Parthenios J, Papagelis K, Riaz I, Jalil R, Novoselov K S and Galotis C 2010 Compression behavior of single-layer graphenes *ACS Nano* **4** 3131–8
- [12] Avouris P and Freitag M 2014 Graphene photonics, plasmonics, and optoelectronics *IEEE J. Sel. Top. Quantum Electron.* **20** 3677–94
- [13] Cooper D R et al 2012 Experimental review of graphene *ISRN Condens. Matter Phys.* **2012** 1–56
- [14] Zhang L, Xia J, Zhao Q, Liu L and Zhang Z 2010 Functional graphene oxide as a nanocarrier for controlled loading and targeted delivery of mixed anticancer drugs *Small* **6** 537–44
- [15] Liu Z, Robinson J T, Sun X and Dai H 2008 PEGylated nanographene oxide for delivery of water-insoluble cancer drugs *J. Am. Chem. Soc.* **130** 10876–7
- [16] Yang X, Zhang X, Liu Z, Ma Y, Huang Y and Chen Y 2008 High-efficiency loading and controlled release of doxorubicin hydrochloride on graphene oxide *J. Phys. Chem. C* **112** 17554–8

- [17] Zhiwei P, Lin J, Ye R, Samuel E L G and Tour J M 2015 Flexible and stackable laser-induced graphene supercapacitors *ACS Appl. Mater. Interfaces* **7** 3414–9
- [18] Castro Neto A H, Peres N M R, Novoselov K S and Geim A K 2009 The electronic properties of graphene *Rev. Mod. Phys.* **81** 109–62
- [19] Sakhaee-Pour A, Ahmadian M T and Vafai A 2008 Potential application of single-layered graphene sheet as strain sensor *Solid State Commun.* **147** 336–40
- [20] Wang Y, Yang R, Shi Z, Zhang L, Shi D, Wang E and Zhang G 2011 Super-elastic graphene ripples for flexible strain sensors *ACS Nano* **5** 3645–50
- [21] Pereira V M and Castro Neto A H 2009 Strain engineering of graphene's electronic structure *Phys. Rev. Lett.* **103** 046801
- [22] Bao W, Miao F, Chen Z, Zhang H, Jang W, Dames C and Lau C N 2009 Controlled ripple texturing of suspended graphene and ultrathin graphite membranes *Nat. Nanotechnol.* **4** 562–6
- [23] Guinea F, Horowitz B and Le Doussal P 2008 Gauge field induced by ripples in graphene *Phys. Rev. B* **77** 205421
- [24] Isacson A, Jonsson L M, Kinaret J M and Jonson M 2008 Electronic superlattices in corrugated graphene *Phys. Rev. B* **77** 035423
- [25] Ni Z H, Yu T, Lu Y H, Wang Y Y, Feng Y P and Shen Z X 2008 Uniaxial strain on graphene: Raman spectroscopy study and band-gap opening *ACS Nano* **2** 2301–5
- [26] Mohiuddin T M G et al 2009 Uniaxial strain in graphene by Raman spectroscopy: G peak splitting, Grüneisen parameters, and sample orientation *Phys. Rev. B* **79** 205433
- [27] Yu T, Ni Z, Du C, You Y, Wang Y and Shen Z 2008 Raman mapping investigation of graphene on transparent flexible substrate: the strain effect *J. Phys. Chem. C* **112** 12602–5
- [28] Vlatts C and Galiotis C 1991 Monitoring the behaviour of polymer fibres under axial compression *Polymer* **32** 1788–93
- [29] Tsoukleri G, Parthenios J, Papagelis K, Jalil R, Ferrari A C, Geim A K, Novoselov K S and Galiotis C 2009 Subjecting a graphene monolayer to tension and compression *Small* **5** 2397–402
- [30] Lu Q and Huang R 2009 Nonlinear mechanics of single-atomic-layer graphene sheets *Int. J. Appl. Mech.* **01** 443–67
- [31] Neek-Amal M and Peeters F M 2010 Defected graphene nanoribbons under axial compression *Appl. Phys. Lett.* **97** 153118
- [32] Neek-Amal M and Peeters F M 2010 Graphene nanoribbons subjected to axial stress *Phys. Rev. B* **82** 085432
- [33] Zhang Y and Liu F 2011 Maximum asymmetry in strain induced mechanical instability of graphene: compression versus tension *Appl. Phys. Lett.* **99** 241908
- [34] Pradhan S C and Murmu T 2009 Small scale effect on the buckling of single-layered graphene sheets under biaxial compression via nonlocal continuum mechanics *Comput. Mater. Sci.* **47** 268–74
- [35] Rees D W A 2009 *Mechanics of Optimal Structural Design: Minimum Weight Structures* (New York: Wiley)
- [36] Chandra Y, Chowdhury R, Adhikari S and Scarpa F 2011 Elastic instability of bilayer graphene using atomistic finite element *Physica E* **44** 12–6
- [37] Plimpton S 1995 Fast parallel algorithms for short-range molecular dynamics *J. Comp. Phys.* **117** 1–19
- [38] LAMMPS Molecular Dynamics Simulator, Available from: (<http://lammps.sandia.gov/>)
- [39] Nosé S 1984 A unified formulation of the constant temperature molecular dynamics methods *J. Chem. Phys.* **81** 511–9
- [40] Hoover W G 1985 Canonical dynamics: equilibrium phase-space distributions *Phys. Rev. A* **31** 1695–7
- [41] Košmrlj A and Nelson D R 2016 Response of thermalized ribbons to pulling and bending *Phys. Rev. B* **93** 125431
- [42] Tersoff J 1988 New empirical approach for the structure and energy of covalent systems *Phys. Rev. B* **37** 6991
- [43] Tersoff J 1989 Modeling solid-state chemistry: interatomic potentials for multicomponent systems *Phys. Rev. B* **39** 5566
- [44] Stuart S J, Tutein A B and Harrison J A 2000 A reactive potential for hydrocarbons with intermolecular interactions *J. Chem. Phys.* **112** 6472–86
- [45] Los J H and Fasolino A 2003 Intrinsic long-range bond-order potential for carbon: performance in Monte Carlo simulations of graphitization *Phys. Rev. B* **68** 024107
- [46] Brenner D W, Shenderova O A, Harrison J A, Stuart S J, Ni B and Sinnott S B 2002 A second-generation reactive empirical bond order (REBO) potential energy expression for hydrocarbons *J. Phys.: Condens. Matter* **14** 783–802
- [47] Koukaras E N, Kalosakas G, Galiotis C and Papagelis K 2015 Phonon properties of graphene derived from molecular dynamics simulations *Sci. Rep.* **5** 12923
- [48] Humphrey W, Dalke A and Schulten K 1996 VMD: visual molecular dynamics *J. Mol. Graph.* **14** 33–8
- [49] Kraus D 2014 Consolidated data analysis and presentation using an open-source add-in for the Microsoft Excel® spreadsheet software *Med. Writ.* **23** 25–8
- [50] Girifalco L A and Lad R A 1956 Energy of cohesion, compressibility, and the potential energy functions of the graphite system *J. Chem. Phys.* **25** 693
- [51] Wagner P, Ivanovskaya V V, Rayson M J, Briddon P R and Ewels C P 2013 Mechanical properties of nanosheets and nanotubes investigated using a new geometry independent volume definition *J. Phys.: Condens. Matter* **25** 155302
- [52] Popov A M, Lebedeva I V, Knizhnik A A, Lozovik Y E and Potapkin B V 2012 Barriers to motion and rotation of graphene layers based on measurements of shear mode frequencies *Chem. Phys. Lett.* **536** 82–6
- [53] Han S M, Benaroya H and Wei T 1999 Dynamics of transversely vibrating beams using four engineering theories *J. Sound Vib.* **225** 935–88
- [54] Kalosakas G, Lathiotakis N N, Galiotis C and Papagelis K 2013 In-plane force fields and elastic properties of graphene *J. Appl. Phys.* **113** 134307
- [55] Gupta S S and Batra R C 2010 Elastic properties and frequencies of free vibrations of single-layer graphene sheets *J. Comput. Theor. Nanosci.* **7** 2151–64
- [56] Liu F, Ming P and Li J 2007 *Ab initio* calculation of ideal strength and phonon instability of graphene under tension *Phys. Rev. B* **76** 064120
- [57] Wei D and Wang F 2014 Graphene: a partially ordered non-periodic solid *J. Chem. Phys.* **141** 144701
- [58] Berinskii I E and Krivtsov A M 2010 On using many-particle interatomic potentials to compute elastic properties of graphene and diamond *Mech. Solids* **45** 815–34
- [59] Androulidakis C, Koukaras E N, Frank O, Tsoukleri G, Sfyris D, Parthenios J, Pugno N, Papagelis K, Novoselov K S and Galiotis C 2014 Failure processes in embedded monolayer graphene under axial compression *Sci. Rep.* **4** 5271
- [60] Zhang D B, Akatyeva E and Dumitrica T 2011 Bending ultrathin graphene at the margins of continuum mechanics *Phys. Rev. Lett.* **106** 255503
- [61] Shibuta Y and Elliott J A 2011 Interaction between two graphene sheets with a turbostratic orientational relationship *Chem. Phys. Lett.* **512** 146–50